J. Fluid Mech. (1982), *vol.* 123, *pp.* 165–185
Printed in Great Britain

On the spectra of high-frequency wind waves

By HSIEN-TA LIU AND JUNG-TAI LIN†
Flow Research Company, Kent, Washington 98031

(Received 4 June 1981 and in revised form 19 March 1982)

Displacements of wind waves in the laboratory were measured with a laser displacement gauge, a recently developed, optical, non-intrusive sensor, which avoids the meniscus effects that severely limit the frequency response of conventional thin-wire gauges. The new gauge is a digital device, which has a maximum frequency response of 2·5 kHz. Its spatial resolution, which depends on the field of view, is typically 0·016 cm for a 4 cm field of view. The wind-wave displacements were measured at several fetches for three wind speeds. Wave-variance spectra derived from these measurements indicate the presence of a quasi-equilibrium spectrum in the capillary-wave regime. The quasi-equilibrium spectrum follows an $f^{-\frac{4}{3}}$ power law that has been predicted on dimensional grounds. The spectral density increases with increasing wind speed from 4 to 10 m/s but is independent of the fetch from 3 to 5 m. In addition, the capillary-wave spectrum is practically unchanged when a relatively long but low-amplitude mechanical wave is superposed onto the wind-generated waves.

1. Introduction

Toward the high-frequency end of the wind-wave spectrum, waves that are controlled partly or entirely by surface tension may be categorized as gravity–capillary and capillary waves. Although the demarcation between them is arbitrary, gravity–capillary waves are usually defined as those with wavelengths between 7 and 0·6 cm and capillary waves are those with wavelengths less than 0·6 cm. The frequencies of 7 and 0·6 cm waves are about 5·0 and 48·5 Hz respectively.

Interest in the dynamic and statistical properties of these waves has recently increased for several reasons. First, there is the need to understand the processes of wind-wave generation and nonlinear energy transfer from short to long waves (Phillips 1966). Secondly, the wind waves in a saturated sea are dissipated through wave breaking, a poorly understood phenomenon. It is clear, however, that wave breaking is a source of capillary waves. The high-frequency waves that are destroyed by viscous dissipation are partly replenished by direct wind generation and through wave breaking. Exactly how capillary waves are generated through wave breaking depends on the strength of the breaking phenomenon. Thirdly, it has recently been demonstrated that high-frequency waves play an important role in using radars for the remote sensing of ocean parameters, such as sea states and friction velocities. Short or Bragg waves that have the same wavelength as the radar signals cause strong

† Present address: United Industries Corporation, 12835 Bellevue/Redmond Road, Bellevue, Washington 98005.

backscattered signals, which may be detected by airborne or spacecraft-based radars (Pierson 1976). The interpretation of these Bragg-scattered signals in terms of the corresponding ocean parameters, however, requires accurate knowledge of the spectral characteristics of the short waves in the presence of long waves. This requirement is the main reason that interest in the measurement of gravity–capillary and capillary waves has dramatically increased.

In the literature, most measurements of wind waves have been conducted in the gravity regime. Accurate measurements of gravity–capillary and capillary waves, especially the latter, are scarce. One reason is that the conventional method, which uses a wave staff, has severe limitations due to the meniscus surface formed around the sensor element and the distortion of the wave field in the presence of the sensor element (Sturm & Sorrell 1973; Kinsman 1965). In an attempt to reduce these limitations, Mitsuyasu & Honda (1974) employed a prewhitening technique to amplify the high-frequency components of the wind waves measured with resistance-wire wave probes (0·1 mm in diameter). Total removal of these limitations, however, requires the use of a non-intrusive or remote sensor.

Several non-intrusive optical methods have been developed for measuring the slopes of high-frequency waves. These include the photographic technique of Cox & Munk (1956) and the refractive technique of Wu (1971). Further refinements of the refractive technique have been made by Long & Huang (1976) and Chang, Wagner & Yuen (1978) for laboratory measurements and by Evans & Shemdin (1980) for ocean-wave measurements. A remote-sensing technique using microwave radars (Larson & Wright 1975) has proved to be very promising for measuring the wavenumber spectra of wind-generated waves. At present, however, the governing equation that is used to relate the Bragg-scattering signals to the surface displacement spectra can only be solved approximately because the equation consists of a nonlinear interaction term that cannot be precisely evaluated. Under certain conditions in which the contribution from the wave–wave interaction is insignificant, the microwave technique is so versatile that it can be used both in the laboratory to study temporal growth rates of wind waves (Larson & Wright 1975) and from space to measure sea surface winds (Young & Moore 1977). A thorough understanding of the wave–wave interaction will be the key to further advances in microwave technique.

Recently, a laser displacement gauge or LDG has been developed by Liu & Lin (1979). The LDG is a non-intrusive technique, which is suitable for measuring displacements of very-high-frequency waves. The present study reports the results of laboratory experiments in which the LDG was used to measure the evolution of the wave-variance spectra in the gravity–capillary and capillary regimes, with and without the presence of a low-amplitude mechanical wave representing a swell. Variations of the spectra, with emphasis in the capillary-wave regime, were observed at two to three fetches for three wind speeds.

In the gravity regime, according to Phillips (1966), an equilibrium range exists in which the peak density E_0 of the spectrum depends on the dominant frequency f_0 as follows:

$$E_0(f_0) \propto f_0^{-5}, \tag{1}$$

as shown by Plate, Chang & Hidy (1969). Furthermore, the envelope of the spectral peaks of the dominant wave and its second harmonics follow the same f_0^{-5} power law (Plate 1977).

In the capillary regime, where surface tension is the dominant force, the wave-variance spectrum $E(f)$ assumes the following asymptotic form, as originally suggested by Hicks (see Phillips 1958), based on dimensional grounds:

$$E(f) = \beta\gamma^{\frac{2}{3}}f^{-\frac{7}{3}} \quad (f_{\mathrm{m}} \ll f \ll f_{\nu}), \tag{2}$$

where β is a constant, γ is the surface tension, f_{m} is the frequency at which the phase speed is a minimum, and f_{ν} is the frequency at which viscous dissipation becomes important. A rough estimate made by Long & Huang (1976) shows that f_{ν} depends on the friction velocity u_*, and is of the order of 10^3 to 10^5 Hz for $u_* = 60$ cm/s. Equation (2) has not been confirmed from laboratory or ocean measurements, mainly because no sensor has been developed to measure displacements of capillary waves with sufficient accuracy. The asymptotic spectrum of the wave slopes in the capillary regime $S_{ij}(f)$, also based on dimensional grounds, is given by (Phillips 1966)

$$S_{ij}(f) = C_{ij}f^{-1} \quad (f_{\mathrm{m}} \ll f \ll f_{\nu}), \tag{3}$$

where C_{ij} is a universal constant tensor, with $i, j = 1, 2$ indicating the slope components in the longitudinal (x) or cross-wind (y) directions respectively. Pierson & Stacy (1973) have proposed that the spectral density in the capillary regime should be dependent on the wind speed or the friction velocity. Their proposed spectrum of the wave displacement in the capillary regime is written as

$$E(f) = 2{\cdot}33 \times 10^{-4} D(u_*)\gamma^{\frac{2}{3}}f^{-\frac{7}{3}}, \tag{4}$$

where $D(u_*)$ is a dimensional parameter, which has been determined empirically by Pierson & Stacy (1973) and Mitsuyasu & Honda (1975). It should be pointed out that in (4) $D(u_*)$, just like β in (2), should be a dimensionless parameter. We will resolve this inconsistency in §4 when we discuss the wind-speed dependence of β.

In the transitional gravity–capillary regime, a spectral form at a frequency somewhat above the gravity equilibrium range was first proposed by Kitaigorodskii (1961):

$$E(f) \simeq Gu_* gf^{-4}, \tag{5}$$

where G is a constant of proportionality and g is the gravitational acceleration. Toba (1973) generalized (5) to include the effect of surface tension:

$$E(f) = (2\pi)^{-3}\alpha_{\mathrm{g}}\, u_* g_* f^{-4}; \tag{6}$$

here α_{g} (approximately 0·02) is a universal constant and $g_* = g + \gamma k^2$, where k is the wavenumber. It is interesting to note that the asymptotic spectrum of wind waves undergoing microscale breaking, as suggested by Phillips (1977), follows an f^{-4} power law. Limited verification of (6) has been made from laboratory data (Mitsuyasu & Honda 1974) and from ocean data (Mitsuyasu 1977). It has been demonstrated that α_{g} increases with the friction velocity. Equation (6) degenerates into (5) in the gravity-dominant regime. In the regime dominated by surface tension, on the other hand, (6) predicts a $-\frac{8}{3}$ instead of a $-\frac{7}{3}$ power law when the asymptotic relation $f = (2\pi)^{-1}(\gamma k^3)^{\frac{1}{2}}$ is used.

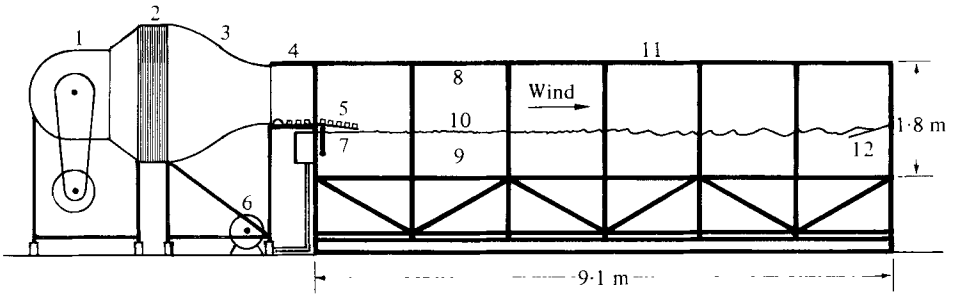

1 Blower
2 Perforated plate and screens
3 Diffuser
4 Flow-conditioning chamber
5 Boundary-layer tripping device
6 Servo-controlled mechanical wave generator
7 Wavemaker
8 Wind tunnel
9 Wave tank
10 Water surface
11 Adjustable ceiling
12 Wave absorber

FIGURE 1. Schematic of the wind-wave facility.

2. Apparatus

The wind-wave tank

Experiments were conducted in a wind-wave tank, which is composed of a wind tunnel on top of a wave tank. Figure 1 is a schematic of the wind-wave tank and accessories; the tank is 9·1 m long, 1·2 m wide and 0·9 m deep. The wind tunnel is open-ended with a blower located at the upwind end. It is suspended over the wave tank, and it has an adjustable ceiling to allow for adjustment of the pressure gradient. The maximum free-stream wind speed that can be obtained is 10 m/s. At the entrance to the wave tank, a boundary-layer tripping mechanism, which consists of a half-cylinder (7·62 cm in diameter), a ramp (20 cm long) and two-dimensional roughness elements (0·32 × 0·32 cm) with 127 cm centre-to-centre spacings, is placed on a 200 cm transition plate. The tripped velocity profiles over wind waves resemble the profiles in a thick turbulent boundary layer (Yu & Lin 1975). The wave tank has transparent sidewalls and a wavemaker installed at the upwind end. The wavemaker is a vertical flap of 20 mm thick Plexiglas, 40 cm high, that spans the wave tank. It is driven by an electrohydraulic servo-control mechanism and is capable of generating surface waves containing single- or multiple-frequency components. A wave absorber is located at the downstream end of the tank to absorb surface waves generated by the wind or the wavemaker. It is a rough, porous, sloping beach, which dissipates the surface-wave energy by causing the waves to break as they run up on the beach and to be drained of energy further by diverting some of the fluid that runs back down the beach through small openings on the beach surface. When the absorber is at an angle of about 10° to the water surface in the tank, the reflection coefficient, defined as the reflected amplitude divided by the incident amplitude, is measured to be less than 5 %. For detailed information on the wind-wave tank see Liu & Lin (1979) and Lin, Gad-el-Hak & Liu (1978).

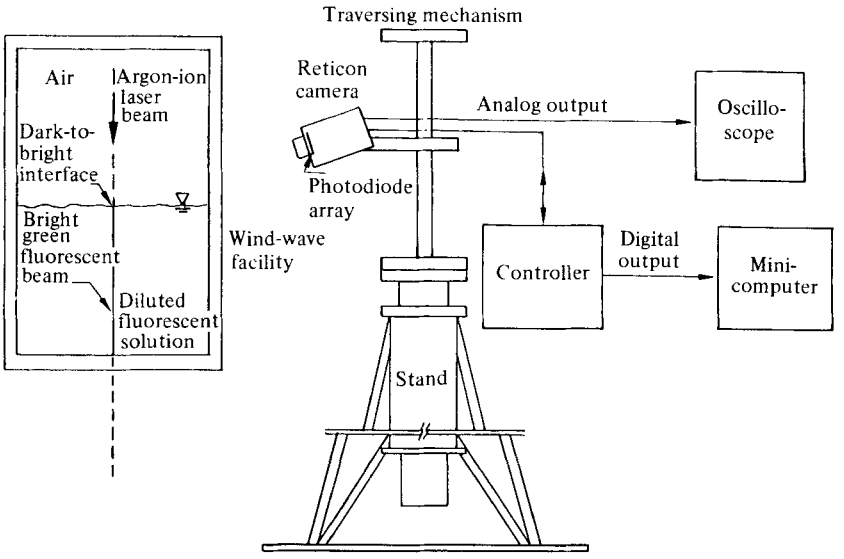

FIGURE 2. Setup of the laser displacement gauge.

System for on-line data acquisition and analysis

The laboratory is equipped with a minicomputer system for on-line data acquisition and analysis. This system consists of a NOVA 800 minicomputer with a 32 k core and peripheral equipment, which includes (i) two magnetic disk drives, an Iomec and a Diablo, each having a 2·5 Mword capacity, (ii) a Wang 9-track, 800-BPI magnetic-tape drive, (iii) a Houston Instrument DPI incremental plotter, (iv) a Versatec model 1100A electrostatic printer–plotter, (v) a Tektronix CRT and hardcopier unit, and (vi) a Teletype. In addition, the computer is equipped with floating-point, integer–multiply–divide, digital–I/O and digital–analog-conversion hardware for analog-input data. A set of computer programs is available for statistical and spectral analysis of the data.

The wave variance spectrum is estimated by performing a fast-Fourier transformation of the autocovariance function of the wave-displacement data. Each time series is divided into eight segments of lengths $\frac{1}{8}N$, where N is the total number of points used for the spectral estimation ($N = 8192$ or 16384 points in our experiments). A sample of the spectrum is estimated from each of the eight segments and then these samples are averaged together to generate the mean spectrum. Furthermore, the spectrum is smoothed by using a Parzen window. Therefore the degree of freedom for the data is 30 and the standard error is estimated to be 26 %. The 95 % confidence limits for the spectrum (Jenkins & Watts 1968) are $[0{\cdot}63E(f), 1{\cdot}78E(f)]$, which are represented by an error bar in the corresponding figures presented later in this paper.

The laser displacement gauge

The key to the present investigation is the successful development of a non-intrusive, optical sensor that is capable of measuring displacements of capillary waves with high accuracy. Detailed descriptions of the laser displacement gauge or LDG and its

operational principles are given elsewhere (Liu & Lin 1979; Lin *et al.* 1978). Figure 2 shows the LDG setup. In essence, an optical interface is created by projecting vertically downward a laser beam about 1 mm in diameter onto the water surface. A 4 W argon-ion laser (Spectra Physics, Model 164-05) is used. The displacement of the surface waves is obtained by measuring the displacement of the optical interface using an electronically self-scanning photodiode array housed in a camera (Reticon Corporation, Model LC600V) and driven by a controller (Reticon Corporation, Model RS605). To enhance the contrast of the optical interface, fluorescein disodium salt is dissolved (approximately 1 p.p.m.) uniformly in the water.

The axis of the photodiode array is aligned with the vertical laser beam above and below the air–water interface. The optical interface is imaged onto the photodiode array via a set of lenses and extension tubes. The photodiode array is composed of 256 elements spaced 25·4 μm centre to centre. The aperture width of the array is also 25·4 μm. The spatial resolution, which is the same in both the vertical and longitudinal directions, depends on the field of view. For example, the spatial resolution is 0·01 cm for a field of view of 2·54 cm. In this case, the horizontal spatial resolution is only about one-tenth of the diameter of the laser beam. The scanning rate of the array ranges from 0·4 to 40 ms. Therefore the LDG has a more than sufficient spatial resolution and frequency response for the measurement of capillary waves. The LDG is a digital device with practically no electronic drift. This is a very important feature when measurement of the absolute displacement of wind waves is called for. The digital output from the controller is a time series of integers from 1 to 256 updated at a frequency of the scanning rate. Each integer corresponds to the nth photodiode on which the optical or air–water interface is imaged during each scan. The digital output is recorded and analysed on-line with the NOVA minicomputer system described above.

Calibration of the LDG is made by displacing the Reticon camera, which is fixed on an accurate traverse mechanism, to several vertical positions with predetermined increments. A second-degree polynomial is best-fitted through the calibration points to account for nonlinearity resulting from the aberration of the optical lenses. We find that the ratio of the coefficients of the nonlinear and linear terms is typically 10^{-4}. For practical purposes, the displacement may be considered to be linearly proportional to the LDG output.

As shown in figure 2, the Reticon camera is mounted so that it looks down onto the water surface at a horizontal angle. This arrangement minimizes blockage of the optical interface by the wave crests between the laser beam and the tank wall on the side where the camera is mounted. This blockage occurs most often near the troughs of the waves, where the wave profiles are relatively smooth. Whenever a blockage occurs, the photodiode array loses its object (i.e. the optical interface) and the maximum diode number of 256 is registered by the controller. Therefore either a sharp jump or a sharp spike, depending on the duration of the blockage, appears on the measured wave profiles. To remove the sharp jumps or spikes, a special program has been written to replace them with a straight line that connects the points before and after each jump or spike.

The performance of the LDG was compared with that of a resistance probe having a 1·6 mm outside diameter with the lower end of the stainless-steel tube plugged. The probe was positioned in close proximity to the laser beam in mechanically generated

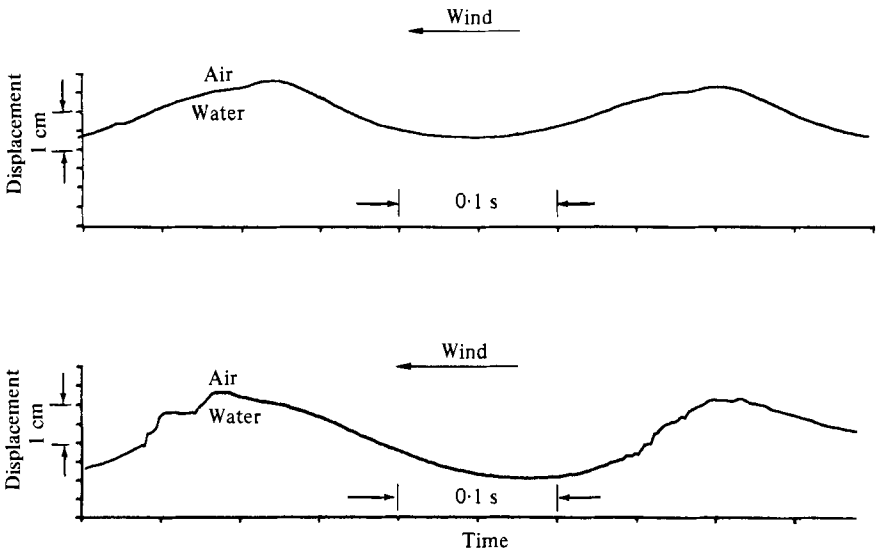

FIGURE 3. Profiles of wind waves measured at a fetch of 5 m and a wind speed of 10 m/s. The top profile was measured with a resistance probe (1·6 mm outside diameter); the bottom profile was measured with the laser displacement gauge. In both, the ordinate and the abscissa have equivalent lengthscales.

waves (Lin *et al.* 1978). The two wave profiles measured with the two instruments agree quite well, except in the regions near wave crests and troughs. The physical disturbance of the wave profile in the presence of the sensor (Kinsman 1965) and the meniscus on the resistance probe (Sturm & Sorrell 1973) distort the wave profiles near the crests and troughs and cause the above discrepancy.

Further comparison of the performances of the two instruments in the measurement of wind-generated waves is presented here. Figure 3 shows two displacement profiles measured at a fetch of 5 m, a wind speed of 10 m/s and a friction velocity of 59·1 cm/s. The top profile was measured with the resistance probe, and the bottom one was measured with the LDG; these profiles were not measured simultaneously or at the same position. The ordinate is the displacement (0·5 cm/division) and the abscissa is the time (0·05 s/division). The horizontal timescale was chosen so that the wave profile has the same lengthscale in the vertical direction as in the horizontal direction. The dominant wavelength was measured to be about 11·2 cm. In the figure, the time increases to the right, and therefore the apparent propagation direction is to the left, as is the wind. Noticeable differences between these two profiles can be seen. First of all, the profile measured with the resistance probe is more symmetrical than that measured with the LDG. The latter profile is skewed to the leeward side of the dominant wave crests, which is consistent with visual observations (e.g. Pierson & Stacy 1973). Most importantly, the wave profile measured with the LDG shows small-scale capillary waves riding on the crests of the dominant waves. The capillary waves are mostly concentrated on the leeward side of the dominant wave crests and are drastically different in shape on the two dominant waves. Small-scale or microscale wave breaking (Phillips 1977) is evident from visual observation of the wind waves and is demonstrated by the extremely steep slope of the capillary waves.

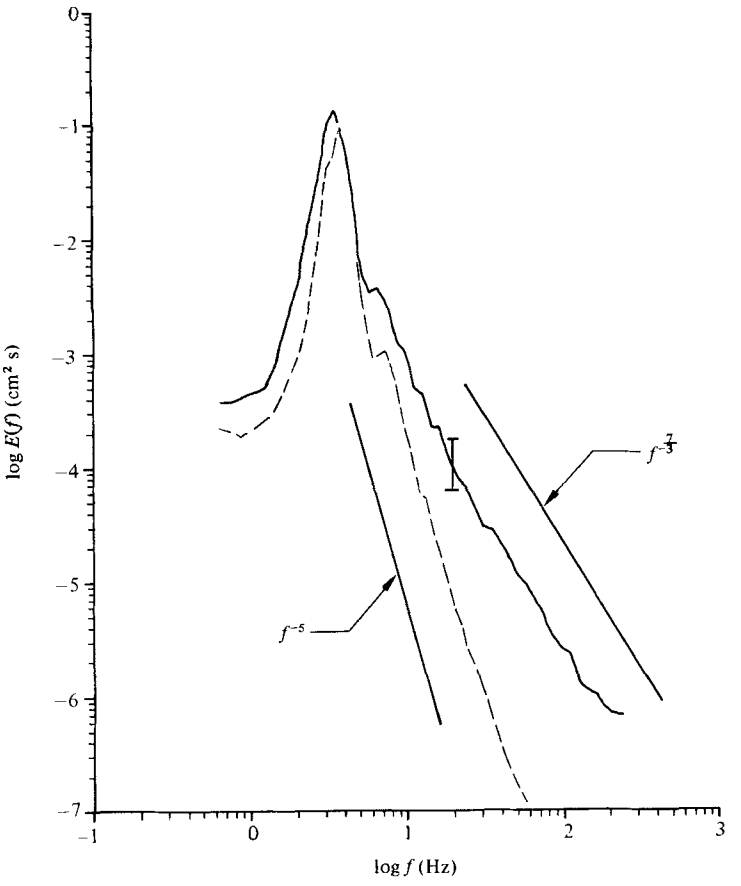

FIGURE 4. Wave variance spectra measured at a fetch of 5 m and a wind speed of 10 m/s. – –, resistance probe (1·6 mm outside diameter); ——, laser displacement gauge.

These capillary-wave features have been observed in other visual results (e.g. Mitsuyasu & Honda 1975) and indicated from slope measurements using a slope gauge (Cox 1958).

Figure 4 shows another comparison in terms of the wave variance spectra calculated from the two time series of wave displacements shown in figure 3. The ordinate and abscissa are respectively the wave variance spectrum and the frequency in hertz. The solid curve represents the spectrum calculated from the wave displacement measured with the LDG, and the dashed curve represents that measured with the resistance probe. The increasingly large deviation of the two curves with the increase of frequency for $f > 6$ Hz is of most interest. The solid curve displays an extensive region (15 Hz $\lesssim f \lesssim$ 200 Hz) in which the spectrum follows an $f^{-\frac{7}{3}}$ power law approximately as illustrated by (2) or (4), whereas the dashed curve shows a -5 power law in the same frequency range. The physical significance of the $-\frac{7}{3}$ power law will be discussed in §3. It is sufficient to say that the incapability of the resistance probe in measuring the small-scale, high-frequency capillary waves is the main contribution to the above-mentioned deviation. Apparently, the meniscus surface

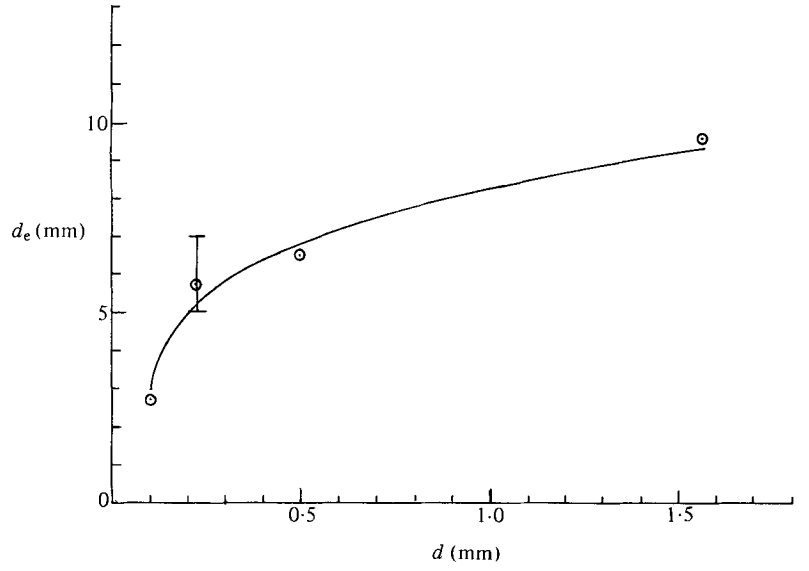

FIGURE 5. Effective diameter of a resistance probe. ○, static meniscus (White & Tallmadge 1965); I, matching diameter of laser beam (Sturm & Sorrell 1973).

surrounding the resistance probe not only distorts the wave profile but also acts like a low-pass filter to the wind-wave signals. The extension of the -5 power law to this high-frequency range is merely a coincidence resulting from the low-pass filtering and it bears no physical significance. It should be pointed out that the equilibrium spectrum in the gravity-wave range follows the -5 power law (Phillips 1966). As a result, the above coincidence has caused confusion in determining the frequency range of the gravity equilibrium spectrum.

Sturm & Sorrell (1973) determined that the effective diameter of a resistance probe 0·224 mm in diameter is about 5–7 mm. The effective diameter, which is defined as the diameter of the meniscus profile where the height is 10 % of the maximum height, was determined by matching the response of the probe to that of an expanded laser beam of a slope gauge similar to that used by Cox (1958). The above range of values agrees with that from static measurements of the height of the meniscus profile by White & Tallmadge (1965). Figure 5 is a plot of the effective diameter d_e versus the probe diameter d, based on the results obtained by Sturm & Sorrell (1973) and White & Tallmadge (1965). As shown in the figure, the effective diameter of a 1·6 mm diameter probe is extrapolated to be about 10 mm. It follows that amplitude attenuation begins to take place for wavelengths less than about 10 cm, which is about the same as the dominant wavelength of the wind waves under consideration. This is consistent with the slightly lower peak spectral density of the dashed curve compared with that of the solid curve shown in figure 4.

In a separate experiment, the performances of the LDG and two thin-wire gauges† (0·13 and 0·41 mm in diameter) placed side by side in the wind–wave facility were

† The two gauges were provided by Dr Kristina Katsaros, Atmospheric Science Department, University of Washington. She used them during the recent MARSEN experiments.

compared (Liu, Katsaros & Weissman 1982). For $f > 15$ Hz, a noticeable discrepancy in the spectral density is observed between the spectra measured with the LDG and the thin wires. The smaller wire performed only slightly better than the larger one. It must be reemphasized that the horizontal spatial resolution of the LDG is limited by the aperture of the photodiode array but not by the diameter of the laser beam. Typically, the spatial resolution, which depends on the field of view, is about 0·1–0·2 mm; the laser-beam diameter used for the measurements reported herein was about 1 mm.

3. Experimental results

The wave variance spectra measured with the LDG at two to three fetches and three wind speeds, with and without a low-amplitude mechanical wave, are presented to determine their effects on the high-frequency components of wind waves. Emphasis is placed on the intermediate-to-high-speed cases in which the air boundary layer is turbulent. The high-frequency waves are generated directly by wind and, at high wind speeds, indirectly through wave breaking. In most cases, the dominant or peak spectral densities of the wind waves have reached the equilibrium level of gravity waves. In other words, the waves are undergoing the second and third stages of growth (Plate *et al.* 1969).

The wave spectra of wind waves measured at a fetch of 5 m for three wind speeds $U = 4$, 7 and 10 m/s are shown in figure 6. The corresponding friction velocities u_* are 20, 39 and 59 cm/s respectively. Details of the velocity profiles in the air and water boundary layers are given elsewhere (Lin *et al.* 1978). For $U = 10$ m/s, the spectra of two independent runs represented by the solid and dotted curves are shown. Excellent repeatability is demonstrated by these two spectra. The envelopes of the spectral peaks and the second harmonics for $U = 7$ and 10 m/s follow an f^{-5} power law. The spectral peak for $U = 4$ m/s is slightly lower than the f^{-5} envelope at the dominant frequency. The increase of the wind speed reduces the dominant frequency but increases the peak spectral density. The f^{-5} envelope, which corresponds to the equilibrium spectrum of gravity waves (Phillips 1966), is consistent with other laboratory results (Plate *et al.* 1969; Mitsuyasu & Rikiishi 1978).

At the high-frequency end, the capillary-wave spectra shown in figure 6 follow a $-\frac{7}{3}$ power law in accord with (2) or (4). For $U = 7$ and 10 m/s, the $-\frac{7}{3}$ power law is observed in a wide frequency range from approximately 15 to 200 Hz. The spectral density in the capillary regime increases, however, with increasing wind speed or friction velocity. The above findings indicate that there exists a quasi-equilibrium spectral range in which the spectrum of capillary waves follows a $-\frac{7}{3}$ power law and the spectral density increases with increasing wind speed or friction velocity.

For $U = 4$ m/s or $u_* = 20$ cm/s, the frequency range in which the $-\frac{7}{3}$ power law is observed is very limited. Beyond $f \simeq 60$ Hz, which corresponds to f_ν as defined in (2) or (3), the spectrum has a slope considerably steeper than $f^{-\frac{7}{3}}$ before it levels off at about 100 Hz. This steep-slope region corresponds to the viscous-cutoff spectral regime, in which viscosity plays an important role in dissipating the high-frequency waves (Pierson & Stacy 1973). The levelling off of the spectrum for $f \gtrsim 100$ Hz bears no physical significance. It is brought about by the finite vertical spatial resolution (approximately 0·01 cm) of the LDG for the particular setup and therefore by

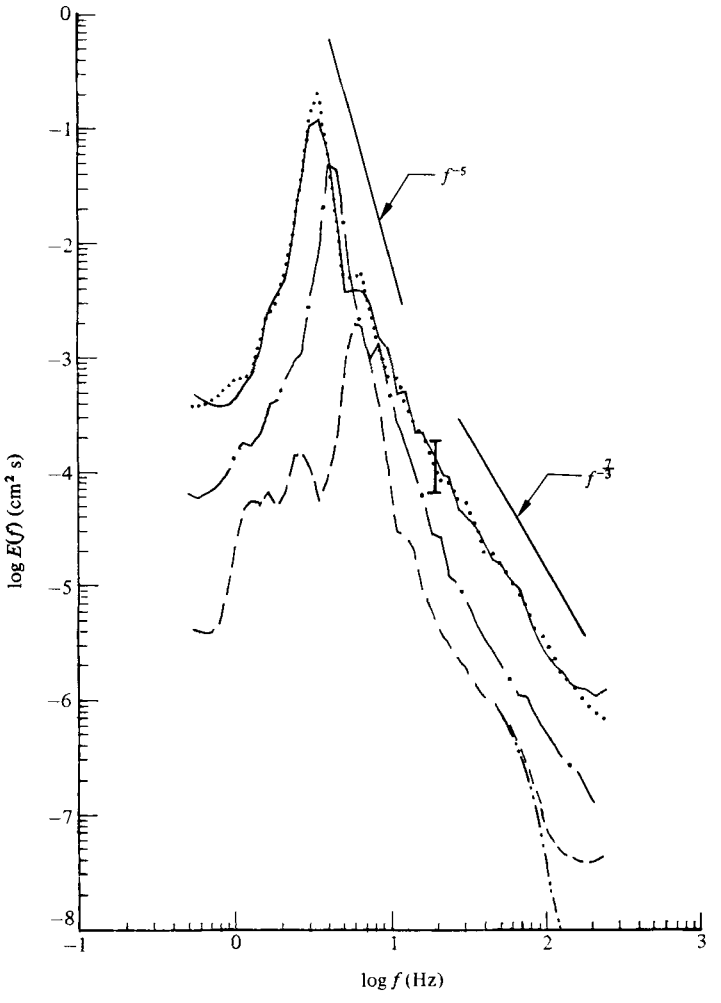

FIGURE 6. Wind-speed effects on wind waves measured at a fetch of 5 m. ——, ... , $U = 10$ m/s; —·—, 7 m/s; - - -, —··— (corrected), 4 m/s.

aliasing. Consequently, a more-gentle slope in the viscous-cutoff range results. For a spatial resolution of 0·01 cm, we have estimated a corresponding noise level in the spectrum to be roughly $3{\cdot}5 \times 10^{-8}$ cm² s. The dash–dot–dot curve in figure 6 represents the corrected spectrum after this estimated noise is subtracted from the original spectrum. This correction extends the viscous-cutoff range to the high-frequency end. To determine the true slope in the viscous-cutoff range, finer spatial resolution (by reducing the field of view of the Reticon camera for small-amplitude waves) is required. Apparently, the frequency f_ν below which the $-\frac{7}{3}$ power law is observed in the wave variance spectrum as defined in (2), is greater for large U or u_*. This finding is consistent with that derived from the slope spectrum measured by Cox (1958). For example, f_ν for $U = 4$ m/s is found to be about 60 Hz from figure 6, whereas f_ν for $U = 3{\cdot}2$ m/s, derived from Cox's data, is about 50 Hz. In figure 6, we find that f_ν is

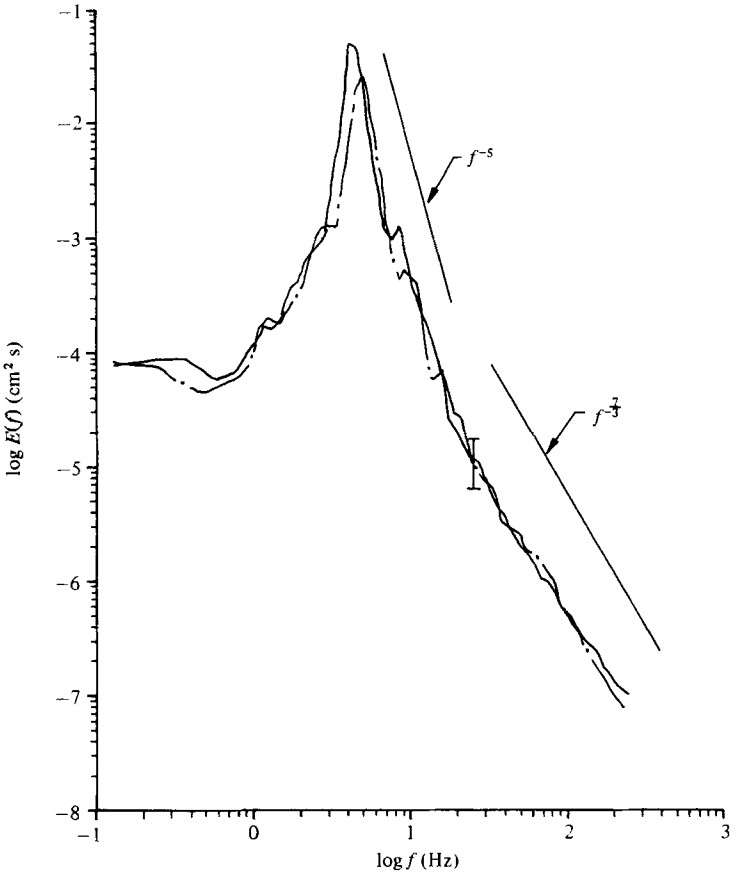

FIGURE 7. Fetch effects on wind waves for a wind speed of 7 m/s. ——, fetch = 5 m; – –, 4 m.

greater than 250 Hz for $U = 7$ and 10 m/s. A higher sampling rate than 500 Hz is required to determine f_ν for these wind speeds. Recently, Liu *et al.* (1982) used the LDG to calibrate the dynamic response of two thin-wire probes with diameters of 0·13 and 0·41 mm. In that experiment, the spatial resolution and the sampling rate of the LDG were selected to be 0·007 cm and 1 kHz respectively. The results have further demonstrated the increase of f_ν with increasing wind speed.

The quasi-equilibrium behaviour of the spectrum in the capillary regime has been observed in the laboratory by other investigators. Mitsuyasu & Honda (1974), who measured wave displacements with thin-wire probes, found that the slope of the spectrum in the capillary regime decreases gradually with increaing wind speed. For $U \lesssim 10$ m/s, however, the slope is generally steeper than $f^{-\frac{7}{3}}$. The steepening of the slope is attributed to the low-pass filtering resulting from the formation of a meniscus surface around the sensor wire, as described previously. Long & Huang (1976) and Plant (1982), who measured wave slopes with a laser slope gauge, found a quasi-equilibrium range in which the slope spectra follow f^{-1}, which is in accord with (3). Beyond 30 Hz, however, the slope spectra measured by Long & Huang (1976) display an f^{-2} behaviour as a possible result of insufficient spatial resolution (approximately 4°) of their laser slope gauge, as pointed out by the authors.

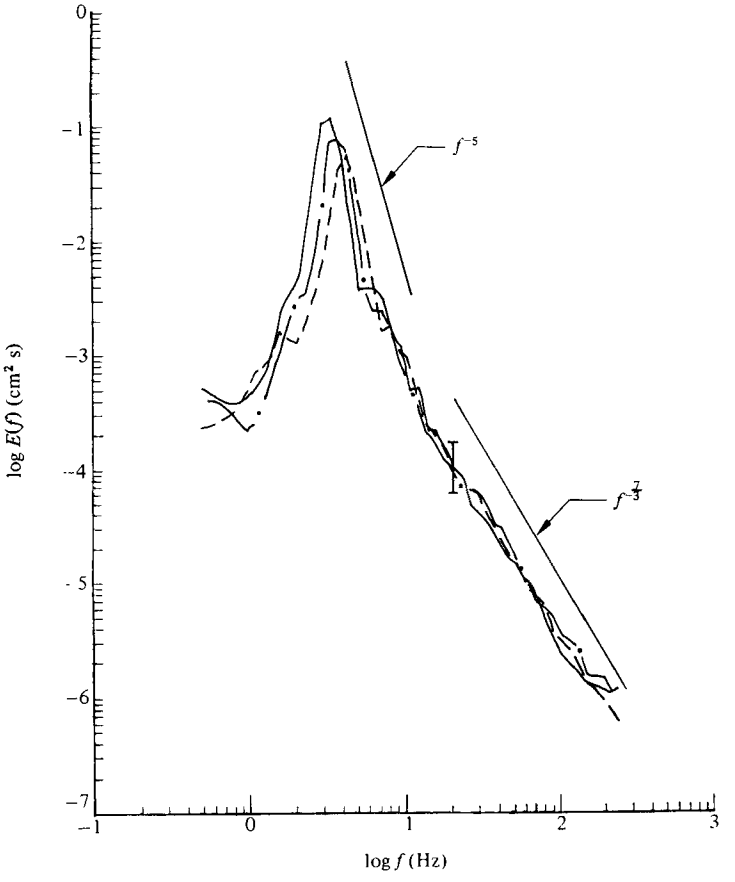

FIGURE 8. Fetch effects on wind waves for a wind speed of 10 m/s. ——, fetch = 5 m; – –, 4 m; - - -, 3·2 m.

Figures 7 and 8 show the spectra of wind waves measured at $x = 4$ and 5 m (where x is the fetch) for $U = 7$ m/s and at $x = 3{\cdot}2$, 4 and 5 m for $U = 10$ m/s. In both figures, the dominant frequency decreases but the spectral peak increases with increasing fetch, as expected. The envelope of the spectral peaks and their second harmonics follows f^{-5}. In the capillary regime, i.e. 15 Hz $\lesssim f \lesssim$ 200 Hz, the spectrum follows $f^{-\frac{7}{3}}$, and is independent of the fetch in the limited range considered herein. Similar findings were derived from the slope spectra for a larger range of fetches (Long & Huang 1976).

The spectra at $x = 3{\cdot}2$, 4 and 5 m for $U = 10$ m/s in the presence of a low-amplitude mechanical wave are illustrated in figure 9. The wave, which was generated by a wave flap, had a frequency of 1·6 Hz, an amplitude of about 2 cm and a wavelength of about 65 cm. For $f > 4$ Hz, the spectrum is independent of the fetch. In the range of about 15 Hz $\lesssim f \lesssim$ 80 Hz, the spectrum follows $f^{-\frac{7}{3}}$. Most importantly, comparison of figures 8 and 9 shows that the spectra with and without the mechanical wave fall onto one another for 10 Hz $\lesssim f \lesssim$ 80 Hz. In other words, the presence of the low-amplitude mechanical wave has practically no influence on the spectrum of the capillary waves except for when $f > 80$ Hz. The deviation from the $-\frac{7}{3}$ power law for $f > 80$ Hz may

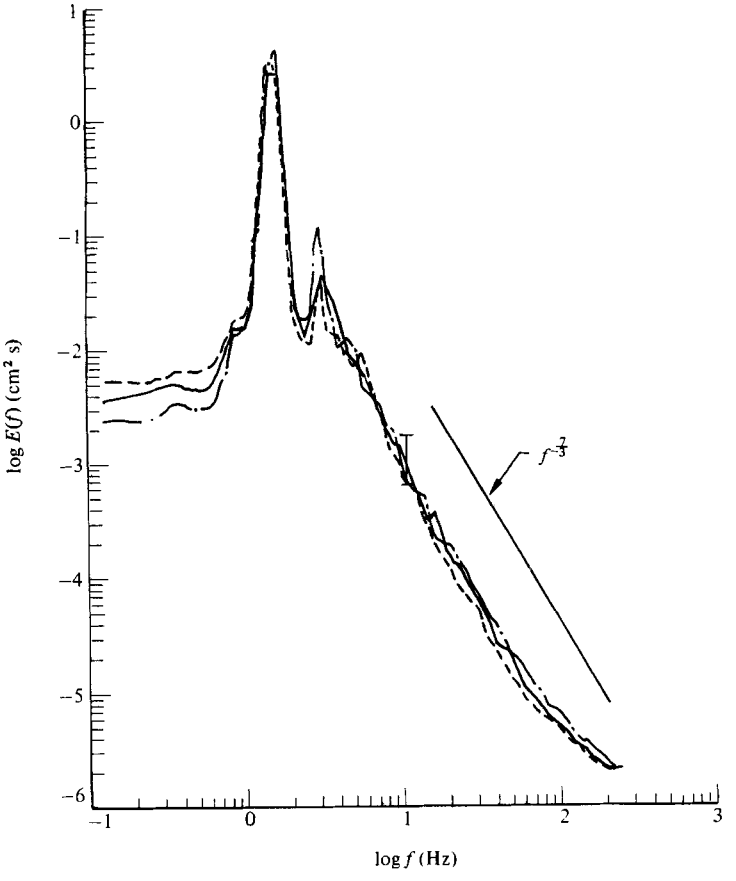

FIGURE 9. Fetch effects on wave variance spectra of wind waves in the presence of a low-amplitude mechanical wave having a frequency of 1·6 Hz and a wave height of about 4 cm. The wind speed is 10 m/s. ——, fetch = 5 m; – –, 4 m; —·—, 3·2 m.

be attributed to the enhancement of wave breaking by the orbital motion of the mechanical wave. Visual records of wind waves (Mitsuyasu & Honda 1975; Pierson & Stacy 1973) have demonstrated that intensive wave breaking introduces a lot of surface fine structure that may be dissipated directly by viscosity or may degenerate into capillary waves and then be dissipated. In another report by the present authors (Lin *et al.* 1978), who introduced intensive wave breaking by 'tripping' the wind waves with large-amplitude mechanical waves, the spectral density in the capillary regime increases while its slope at the high-frequency end decreases with increasing intensity of wave-breaking.

Between the gravity and capillary regimes, figures 6–9 demonstrate the existence of a transitional regime in which the spectrum varies from f^{-5} to $f^{-\frac{7}{3}}$. The frequency range in which the spectrum may take the form of (5) or (6) is, however, very limited. Just like the spectrum in the capillary regime, the spectral density in the gravity–capillary regime increases with increasing U or u_*. This trend is consistent with the u_* dependence in (5) and (6).

In summary, the results presented in this section indicate the existence of a quasi-equilibrium spectral range in the capillary regime. The spectrum in the quasi-equilibrium range has the following characteristics. The spectrum follows an $f^{-\frac{7}{3}}$ power law. The spectral density increases with increasing wind speed or friction velocity, but is apparently independent of the fetch. In the presence of a low-amplitude mechanical wave simulating a swell, the spectrum does not seem to be influenced, except that enhancement of the wave-breaking activity appears to increase the spectral density at the very-high-frequency end, thus reducing its slope to be less than the $f^{-\frac{7}{3}}$ slope. The implications of these important findings will be discussed in §4.

4. Discussion

The increase of the spectral density in the capillary regime with increasing wind speed involves several processes, which probably occur simultaneously but in differing proportions at different wind speeds. First of all, there is the direct generation of capillary waves by the wind whenever the critical wind speed is exceeded (Plate *et al.* 1969). Instability theories in a laminar shear flow (Miles 1962; Valenzuela 1976) predict that the wavelength of the fastest-growing waves decreases with increasing u_*. The critical u_* are 4·4 and 17·5 cm/s on a clear and a slick-covered water surface respectively. The wavelength of the first excited waves on a clear water surface is approximately 3·5 cm; the corresponding frequency is approximately 7·4 Hz. Similarly, Phillips (1967) predicts that the initial ripples generated by resonance with the atmospheric turbulent pressure fluctuations are rhombic waves with a wavelength of 1·7 cm; the corresponding frequency is approximately 13·5 Hz. Furthermore, the same predictions imply that f_ν in (2) or (4) increases with increasing U, consistent with the finding by Cox (1958) and Liu *et al.* (1982).

For medium wind speeds, some of the short gravity waves may reach their maximum steepness. The generation of parasitic capillary waves by the nonlinear interaction of steep, short gravity waves (Longuet-Higgins 1963; Crapper 1970; Chang *et al.* 1978) may contribute significantly to the capillary-wave spectrum. These parasitic waves, which are concentrated in the forward side of the gravity-wave crest, do not disrupt the thin thermal conductive layer on the water surface.

For higher wind speeds, microscale wave breaking, with the surface overturning at small increments in the water surface but without air entrainment, becomes an increasingly important contributor to the capillary-wave spectrum. Unlike the parasitic capillary waves, microscale breaking disrupts the thin thermal conductive layer at the water surface and enhances mass and heat transfers across the air–water interface.

For yet higher wind speeds, transient, sporadic, larger-scale wave breaking (spilling breakers) dominates the other processes. The action of the intensive breaking that entrains air locally (whitecapping) generates a lot of surface fine structure. The surface fine structure may result in capillary waves or may be directly dissipated by viscosity.

All the above processes involve timescales within the period of the dominant waves. They are classified by Phillips (1977) as 'strong' interactions, in contrast to the weak, resonant, nonlinear interactions such as the Benjamin–Feir instability (Benjamin & Feir 1967), which has a timescale much larger than the period of the dominant waves.

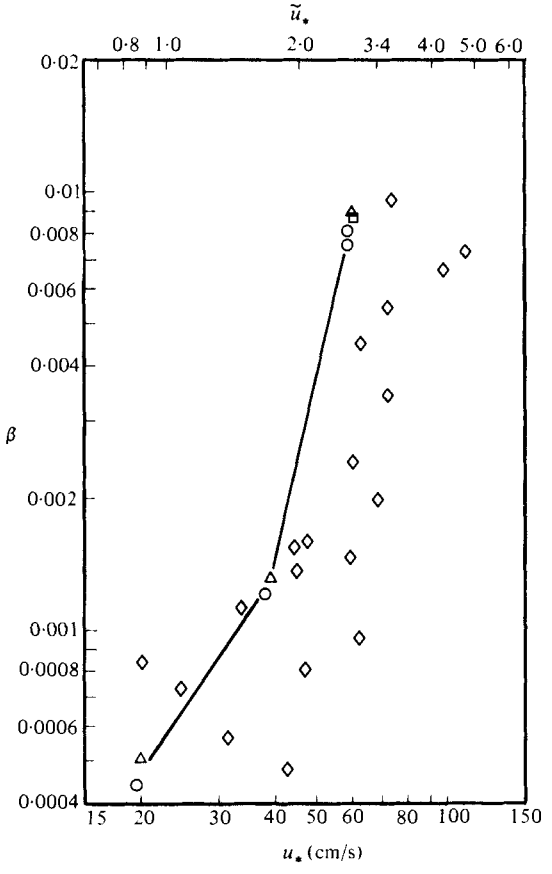

FIGURE 10. Variation of β with u_* or $\tilde{u}_*$. ——, present data, □ = 3·2 m fetch, △ = 4 m, ○ = 5 m; ◇, Mitsuyasu & Honda (1974), measured with 0·1 mm diameter thin wire at five fetches from 1·05 to 8·25 m.

Each of the above processes provides a mechanism for local energy loss from the dominant gravity waves. Visual records of wind waves have demonstrated that the surface fine structure generated by these above processes is distributed nonuniformly in patches on the water surface (Pierson & Stacy 1973; Mitsuyasu & Honda 1975). As the wind speed picks up, the number density and the intensity of the surface fine structure in each patch, as well as the patch size, increase simultaneously, leading to the increase in the spectral density of capillary waves.

The dependence of the quasi-equilibrium spectrum of capillary waves on the wind speed or the friction velocity deserves further discussion. In the context of the increase of the spectral density with increasing wind speed, it is indicative that β in (2) is a function of u_* rather than a universal constant. From dimensional consideration, however, β must be a dimensionless parameter. In other words, the argument of β should combine u_* and other variables, such as the surface tension, $\hat{T}$, to form a dimensionless parameter. Dimensional analysis suggests that the most relevant parameter for capillary waves is the Weber number, which is defined as $\rho u_*^2 L/\hat{T}$, where L is a characteristic length. We may replace L by L_m, the wavelength of the

capillary wave whose phase speed $c_m = (4\pi\hat{T}/\rho L_m)^{\frac{1}{2}}$ has the minimum value (Kinsman 1965). For tap water having a surface tension of 72 dyn/cm, the value of c_m is about 23·1 cm/s. The Weber number may then be expressed as $4\pi u_*^2/c_m^2$. This leads to our proposition that β is a function of the dimensionless friction velocity $\tilde{u}_* = u_*/c_m$, or

$$\beta = \beta(\tilde{u}_*). \tag{7}$$

From the data presented in §3, the estimated variation of β with the friction velocity u_* or $\tilde{u}_*$ is illustrated in figure 10. The solid lines simply connect the three sets of data obtained for the three wind speeds $U = 4$, 7 and 10 m/s. The value of β was estimated from the formula $\beta = E^*(1)\gamma^{-\frac{2}{3}}$ according to (2), where $E^*(1)$ is the intersection of the envelope of the $f^{-\frac{7}{3}}$ spectrum with the vertical axis at $f = 1$ Hz. The increase of β with increasing $\tilde{u}_*$ is clearly noted in the figure. A similar trend is observed for $\partial\beta(\tilde{u}_*)/\partial\tilde{u}_*$. Such a trend is consistent with the discussion at the beginning of this section on the generation processes of capillary waves as a function of increasing wind speed. From figure 10, we find that the effects of the fetch are insignificant compared with those of the wind speed, although more data are required to derive an empirical formula for (7).

Corresponding results derived from measurements with thin-wire probes at five fetches from 1·05 to 8·25 m are also plotted in figure 10 (Mitsuyasu & Honda 1974). Because their spectra do not show a consistent $-\frac{7}{3}$ power law in the capillary regime for different u_*, the value of β was computed differently as

$$\beta = \frac{\gamma^{-\frac{2}{3}}}{f_c - 3f_m}\int_{3f_m}^{f_c} E(f) f^{\frac{7}{3}} df, \tag{8}$$

where f_c, the cutoff frequency, is 50 Hz, and f_m is the dominant frequency. Mitsuyasu & Honda (1974) actually computed $D(u_*)$ in the wavenumber space by first converting the frequency spectrum into the wavenumber spectrum, based on the dispersion relation

$$f(k) = (2\pi)^{-1}(gk + \gamma k^3)^{\frac{1}{2}}. \tag{9}$$

They derived an empirical relation by fitting over the data measured at the five fetches:

$$D(u_*) = 1{\cdot}0 \times 10^{-3} u_*^{\frac{9}{4}} \tag{10}$$

or

$$\beta(\tilde{u}_*) = 2{\cdot}73 \times 10^{-4} \tilde{u}_*^{\frac{9}{4}}, \tag{11}$$

when we relate $\beta(\tilde{u}_*)$ to $D(u_*)$ through (2), (4), (7) and (10). A much larger dependence of the fetch on β than in the present results is observed in the results derived by Mitsuyasu & Honda (1974). By and large, the values of β derived from the present results are larger than those derived from the thin-wire probe measurements (Mitsuyasu & Honda 1974). Evidently, the meniscus effects reduce the spectral density measured by the thin-wire probes in the capillary regime, thus resulting in relatively low β values.

There are two implications of the observed insensitivity of the capillary-wave spectrum to the superposition of a mechanical wave. The first implication, which is of great importance to the remote sensing of the ocean surface with radars, is the apparently small influence of the swell on the capillary spectrum. The second implication relates to the proper simulation of ocean wind waves in a wind–wave tank. There has been evidence that the ocean waves are predominantly composed of free

waves, whereas wind waves generated in the laboratory are often composed of bound waves (Ramamonjiarisoa & Coantic 1976; Donelan, Hamilton & Hui 1980). Donelan *et al.* demonstrated that whether the wind–wave field is predominantly composed of free or bound waves depends on the ratio of c_0 to u_*, where c_0 is the phase speed of the dominant waves. From the dispersion relation derived from both ocean and laboratory data, they show that the wind–wave field is predominantly composed of free waves for $c_0/u_* \gtrsim 2{\cdot}5$. On the other hand, the wind–wave field contains bound high-frequency components for $c_0/u_* \lesssim 1{\cdot}3$. The above finding indicates that the nonlinear behaviour of bound waves is frequently observed when the waves are 'overdriven' by the wind, as are most waves generated in a wind–wave tank. The superposition of a mechanical wave (much longer than the dominant wind wave) on the wind waves is a simple way of increasing the value of c_0/u_*. In the presence of the 1·6 Hz mechanical wave, the value of c_0/u_* for $U = 10$ m/s is about 1·8, provided that the amplitude of the mechanical waves is sufficiently low and that u_* changes insignificantly over the combined wave field. Note that the value of c_0/u_* is about 0·7 without the mechanical wave. Either with a longer mechanical wave or lower wind speed, c_0/u_* will exceed the critical value of 2·5 that is required for the wave field to be predominantly composed of free waves. Correct simulation of ocean waves, however, requires wide-banded waves that fill in the low-frequency portion of the wave spectrum. Our laboratory is equipped with a programmable mechanical wave generator that is capable of generating such wide-banded waves up to about 4 Hz.

To examine the validity of (6) in the gravity–capillary regime, the normalized spectra $(2\pi)^3 E(f) f^4/u_* g_*$ are plotted against f in figure 11 for $U = 7$ and 10 m/s at $x = 4$ and 5 m. Owing to the lack of information on the effects of the drift current, the linear dispersion relation (9) is assumed. At the low-frequency end, the normalized spectral density rises abruptly to a maximum at the dominant frequency. Above the dominant frequency, the normalized spectrum oscillates a few times, levels off and rises roughly as $f^{\frac{1}{3}}$ at the high-frequency end. The gravity–capillary regime coincides with the narrow levelling-off region in which the normalized spectral density, or α_g in accord with (6), is almost a constant. The value of α_g, however, increases with increasing U or u_*, which is consistent with the findings reported by Mitsuyasu & Honda (1974). Because of the small separation in frequency between the dominant wave and the gravity–capillary waves due to limited fetch, the spectrum at the low end of the gravity–capillary regime is masked by the presence of the higher harmonics of the dominant wave. For ocean waves, Mitsuyasu (1977) has shown that the gravity–capillary regime extends to as low as about 5 Hz. From figure 11, the values of α_g are estimated to be about 0·02–0·024 for $U = 10$ m/s or $u_* \simeq 60$ cm/s and 0·008 for $U = 7$ m/s or $u_* \simeq 40$ cm/s. These values are slightly higher than those estimated by Mitsuyasu & Honda (1974) in the same range of fetches. Note that they estimate the value of α_g using the formula

$$\alpha_g = \frac{1}{f_c - 3f_m} \int_{3f_m}^{f_c} [(2\pi)^3 E(f) f^4/u_* g_*]\, df, \tag{12}$$

where the range of the integration corresponds to that in (8).

The frequency at which the slope of the normalized spectrum changes from f^0 to $f^{\frac{1}{3}}$ marks the transition from the gravity–capillary regime to the capillary regime. Note that the $f^{\frac{1}{3}}$ slope is the product of the measured $E(f)$, which follows $f^{-\frac{7}{3}}$ in the capillary

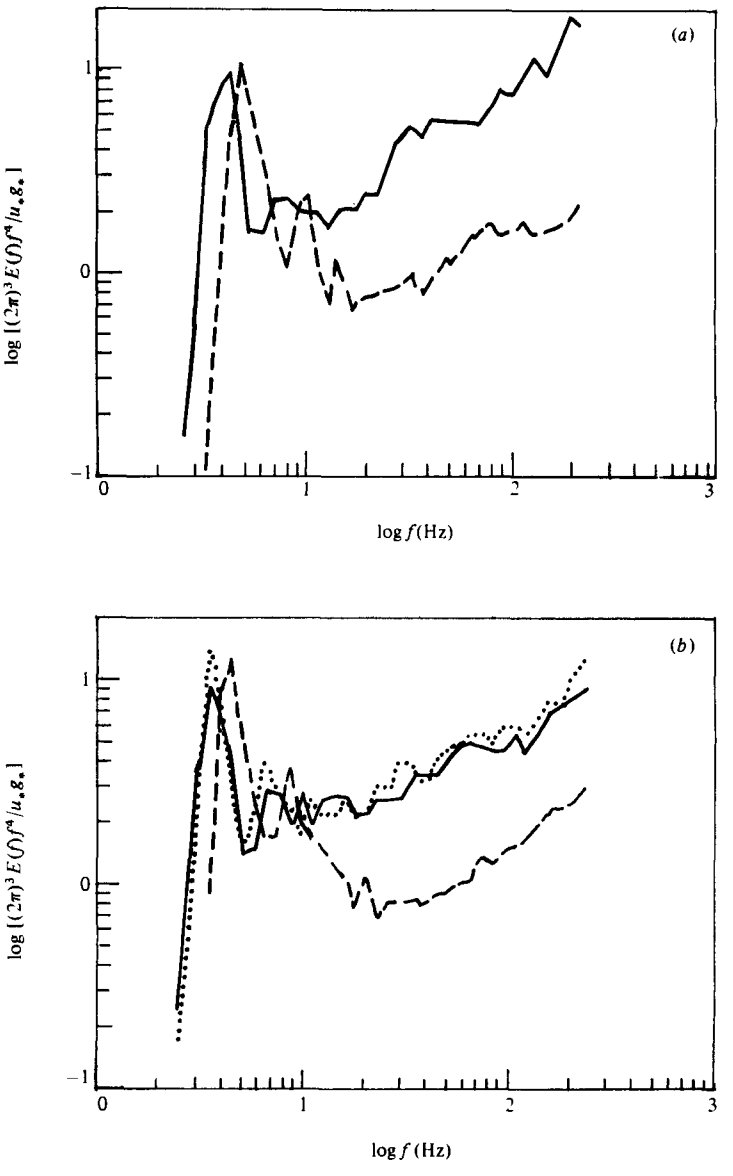

FIGURE 11. Normalized spectra of wind waves. (*a*) Fetch = 4 m; (*b*) fetch = 5 m. ——, ... , $U = 10$ m/s and $u_* \simeq 60$ cm/s; ---, $U = 7$ m/s and $u_* \simeq 40$ cm/s.

regime, and the normalized parameter $(2\pi)^3 f^4/u_* g_*$, which has an asymptotic form of $f^{\frac{5}{2}}$ (see §1). Figure 11 shows that the frequency at which the above transition is observed decreases with increasing U. In other words, the capillary regime extends to a lower frequency as the wind speed increases. It is evident from both field and laboratory data that, for a given wind speed, the maximum frequency range of the gravity–capillary regime is not expected to exceed one-half of a decade. The normalized spectra measured by Mitsuyasu & Honda (1974) using thin-wire probes

do not show a consistent rise in the capillary regime because of the low-pass filtering by the meniscus. Toward the high-frequency end in the viscous-cutoff wave regime, we anticipate that the slopes of the curves in figure 11 will change direction (negative slopes) because the spectrum in the regime falls off steeper than f^{-4} (Liu *et al.* 1982; Pierson 1976).

The authors wish to express their appreciation for the assistance provided by Messrs Randy Srnsky and Glenn Geithman during the experimental phase of the study. This study is partly supported by the U.S. Coast Guard, the U.S. Department of Transportation under Contract no. DOT-CG-61688-A and by a Flow Research IR&D Project.

REFERENCES

BENJAMIN, T. B. & FEIR, J. E. 1967 The disintegration of wave trains on deep water. Part 1. Theory. *J. Fluid Mech.* **27**, 417–430.

CHANG, J. H., WAGNER, R. N. & YUEN, H. C. 1978 Measurement of high frequency capillary waves on steep gravity waves. *J. Fluid Mech.* **86**, 401–413.

COX, C. S. 1958 Measurement of slopes of high frequency wind waves. *J. Mar. Res.* **16**, 199–225.

COX, C. S. & MUNK, W. H. 1954 Measurements of the roughness of the sea surface from photographs of the sun's glitter. *J. Opt. Soc. Am.* **44**, 838–850.

CRAPPER, G. D. 1970 Non-linear capillary waves generated by steep gravity waves. *J. Fluid Mech.* **40**, 149–159.

DONELAN, M. A., HAMILTON, J. & HUI, W. H. 1980 Directional spectra of wind-generated waves. In preparation. (Also paper presented at AMS 3rd Conf. on Ocean–Atmosphere Interaction, Los Angeles, 30 January – 1 February).

EVANS, D. D. & SHEMDIN, O. H. 1980 An investigation of the modulations of capillary and short gravity waves in the open ocean. *J. Geophys. Res.* **85**, 5019–5024.

JENKINS, G. M. & WATTS, D. G. 1968 *Spectral Analysis and Its Applications.* Holden-Day.

KINSMAN, B. 1965 *Wind Waves: Their Generation and Propagation on the Ocean Surface.* Prentice-Hall.

KITAIGORODSKII, S. A. 1961 Applications of the theory of similarity to the analysis of wind generated wave motions as a stochastic process. *Izv. Geophys. Ser. Acad. Sci., USSR* **1**, 105–117. no. 1, 73–80.

LARSON, T. R. & WRIGHT, J. W. 1975 Wind-generated gravity–capillary waves: laboratory measurements of temporal growth rates using microwave backscatter. *J. Fluid Mech.* **70**, 417–436.

LIN, J.-T., GAD-EL-HAK, M. & LIU, H.-T. 1978 A study to conduct experiments concerning turbulent dispersion of oil slicks. *U.S. Coast Guard Rep.* no. CG-D-54-78; NTIS no. AD A058802.

LIU, H.-T., KATSAROS, K. B. & WEISSMAN, M. A. 1982 Dynamic response of thin-wire wave gauges. *J. Geophys. Res.* **87**, 5686–5698.

LIU, H.-T. & LIN, J.-T. 1979 Effect of an oil slick on wind waves. In *Proc. 1979 Oil Spill Conference, Los Angeles*, pp. 665–674. Am. Petroleum Inst.

LIU, H.-T. & LIN, J.- T. 1980 Laboratory studies on breaking waves. Presented at the AMS Third Conf. on Ocean–Atmosphere Interaction, Los Angeles, 30 January–1 February (abstract only).

LONG, S. R. & HUANG, N. E. 1976 On the variation and growth of wave-slope spectra in the capillary–gravity range with increasing wind. *J. Fluid Mech.* **77**, 209–228.

LONGUET-HIGGINS, M. S. 1963 The generation of gravity waves by steep capillary waves. *J. Fluid Mech.* **16**, 138–159.

MILES, J. W. 1962 On the generation of surface waves by shear flows. *J. Fluid Mech.* **13**, 433–448.

MITSUYASU, H. 1977 Measurement of the high-frequency spectrum of ocean surface waves. *J. Phys. Oceanogr.* **7**, 882–891.

MITSUYASU, H. & HONDA, T. 1974 The high-frequency spectrum of wind-generated waves. *J. Oceanogr. Soc. Japan* **30**, 185–198.

MITSUYASU, H. & HONDA, T. 1975 The high-frequency spectrum of wind-generated waves. *Rep. Res. Inst. Appl. Mech.* **22**, 327–355.

MITSUYASU, H. & RIKIISHI, K. 1978 The growth of duration-limited wind waves. *J. Fluid Mech.* **85**, 705–730.

PHILLIPS, O. M. 1958 On some properties of the spectrum of wind-generated ocean waves. *J. Mar. Res.* **16**, 231–245.

PHILLIPS, O. M. 1966 *The Dynamics of the Upper Ocean.* Cambridge University Press.

PHILLIPS, O. M. 1967 On the generation of waves by turbulent wind. *J. Fluid Mech.* **2**, 417–445.

PHILLIPS, O. M. 1977 Strong interaction in wind–wave fields. *Air–Sea Interaction 1, NATO Conf. Ser.* no. 5, pp. 373–384.

PIERSON, W. J. 1976 The theory and application of ocean wave measuring systems at and below sea surface on the land, from the aircraft and from spacecraft. *NASA Contractor Rep.* no. CR-2646.

PIERSON, W. J. & STACY, R. A. 1973 The elevation, slope, and curvature spectra of wind roughened sea surface. *NASA Contractor Rep.* no. CR-2247.

PLANT, W. J. 1982 A relationship between wind stress and wave slope. *J. Geophys. Res.* **87**, 1961–1967.

PLATE, E. J. 1977 Wind-generated water surface waves: the laboratory evidence. *Air–Sea Interaction 1, NATO Conf. Ser.* no. 5, pp. 385–401.

PLATE, E. J., CHANG, P. C. & HIDY, G. M. 1969 Experiments on the generation of small water waves by wind. *J. Fluid Mech.* **35**, 625–656.

RAMAMONJIARISOA, A. & COANTIC, M. 1976 Loi expérimentale de dispersion des vagues produites par le vent sur une faible longueur d'action. *C. R. Acad. Sci. Paris* B **282**, 111–113.

STURM, G. V. & SORRELL, F. Y. 1973 Optical measurement technique and experimental comparison with wave height probes. *Appl. Opt.* **12**, 1928–1933.

TOBA, Y. 1973 Local balance in the air–sea boundary process III. *J. Oceanogr. Soc. Japan* **29**, 209–225.

VALENZUELA, G. R. 1976 The growth of gravity–capillary waves in a coupled shear flow. *J. Fluid Mech.* **76**, 229–250.

WHITE, D. A. & TALLMADGE, J. A. 1965 Static menisci on the outside of cylinders. *J. Fluid Mech.* **23**, 325–336.

WU, J. 1971 Slope and curvature distributions of wind-disturbed water surface. *J. Opt. Soc. Am.* **61**, 852–858.

YOUNG, J. D. & MOORE, R. K. 1977 Active microwave measurement from space of sea-surface winds. *IEEE J. Ocean Engng* OE-**2**, 309–317.

YU, H. Y. & LIN, J.-T. 1975 A technique for generating a turbulent boundary layer in a wind-wave tank. In *Proc. 2nd U.S. Nat. Conf. on Wind Engineering Research, Colorado State University, Ft Collins*, pp. IV.3.1–4.